Nano Research
2019, 12(3): 683–693

ISSN 1998-0124 CN 11-5974/O4
https://doi.org/10.1007/s12274-019-2277-z

Research Article

Novel highly active carbon supported ternary PdNiBi nanoparticles as anode catalyst for the alkaline direct ethanol fuel cell

Bernd Cermenek[1] (✉), Johanna Ranninger[1], Birgit Feketeföldi[2], Ilse Letofsky-Papst[3], Norbert Kienzl[4], Brigitte Bitschnau[5], and Viktor Hacker[1] (✉)

[1] *Institute of Chemical Engineering and Environmental Technology, Graz University of Technology, NAWI Graz, Inffeldgasse 25/C, 8010 Graz, Austria*
[2] *Institute for Surface Technologies and Photonics, JOANNEUM RESEARCH Forschungsgesellschaft mbH/Materials, Franz-Pichler-Straße 30, 8160 Weiz, Austria*
[3] *Institute for Electron Microscopy and Nanoanalysis and Center for Electron Microscopy, Graz University of Technology, NAWI Graz, Steyrergasse 17, 8010 Graz, Austria*
[4] *Bioenergy 2020+ GmbH, Inffeldgasse 21/B, 8010 Graz, Austria*
[5] *Institute of Physical and Theoretical Chemistry, Graz University of Technology, Streymayrgasse 9, 8010 Graz, Austria*

Received: 14 October 2018 / **Revised:** 16 December 2018 / **Accepted:** 21 December 2018

ABSTRACT

The study focuses on the influence of Ni and Bi on alkaline ethanol oxidation reaction (EOR) activities, stabilities and structure characteristics of carbon supported Pd-based nanocatalysts (Pd/C, $Pd_{60}Ni_{40}$/C, $Pd_{60}Bi_{40}$/C, $Pd_{60}Ni_{20}Bi_{20}$/C) by cyclic voltammetry/chronoamperometry using rotating disk electrode and various physico-chemical methods such as X-ray powder diffraction, X-ray photoelectron spectroscopy, transmission electron microscopy coupled with energy dispersive X-ray spectroscopy and inductively coupled plasma optical emission spectrometry. Nickel generates more adsorbed OH on the Pd catalyst surface than Bi and promotes the oxidation of adsorbed ethanol species. This results in a low onset potential toward ethanol oxidation with high current density. The presence of Bi facilitates high tolerance toward various reaction intermediates resulting from the incomplete ethanol oxidation, but might also initiate the agglomeration of Pd nanoparticles. The novel $Pd_{60}Ni_{20}Bi_{20}$/C nanocatalyst displays exceptional byproduct tolerance, but only satisfying catalytic activity toward ethanol oxidation in an alkaline medium. Therefore, the EOR performance of the novel carbon supported ternary $Pd_xNi_yBi_z$ anode catalyst with various atomic variations ($Pd_{70}Ni_{25}Bi_5$/C, $Pd_{70}Ni_{20}Bi_{10}$/C, $Pd_{80}Ni_{10}Bi_{10}$/C and $Pd_{40}Ni_{20}Bi_{40}$/C) using the common instant reduction synthesis method was further optimized for the alkaline direct ethanol fuel cell. The carbon supported Pd:Ni:Bi nanocatalyst with atomic ratio of 70:20:10 displays outstanding catalytic activity for the alkaline EOR compared to the other $Pd_xNi_yBi_z$/C nanocatalysts as well as to the benchmarks Pd/C, $Pd_{60}Ni_{40}$/C and $Pd_{60}Bi_{40}$/C. The synergy and the optimal content in consideration of the oxide species of Pd, Ni and Bi are crucial for the EOR kinetic enhancement in alkaline medium.

KEYWORDS

alkaline direct ethanol fuel cell, catalytic activity, ethanol oxidation reaction, ternary PdNiBi nanocatalysts, structure characteristics

1 Introduction

The alkaline direct ethanol fuel cell (ADEFC) using non-Pt-based electrocatalysts, and cost-efficient materials to produce anion exchange membranes (AEMs), is a low-cost, environment-friendly and easy-handling energy source as an alternative to batteries for small-scale portable applications [1].

The ADEFC exhibits the following benefits compared to other low temperature fuel cells:

1) Ethanol is a sustainable, low-toxic, liquid fuel with high volumetric energy density (6.3 kWh·L^{-1}) compared to methanol (4.8 kWh·L^{-1}) and hydrogen (2.6 kWh·L^{-1}) and thereby easy to handle, store and transport [1–6].

2) The production of ethanol from agricultural products or biomass e.g. straw, corn, sugar cane or wheat compared to methanol and hydrogen avoids the use of limited availability fossil fuels as feedstocks [3, 5].

3) The usage of alkaline electrolytes leads to the following improvements: a) The kinetics of ethanol oxidation reaction (EOR) and oxygen reduction reaction (ORR) are enhanced [1–6]. b) Non-noble elements (e.g. Ni, Fe, Co, Bi or Mn) as admetals are used for the production of EOR and ORR catalysts to reduce the catalytic material costs and to enhance their catalytic performance [1–9]. c) The use of the AEM instead of the cation exchange membrane (CEM) lowers the costs (AEM: 67.5 \$·m^{-2} vs. CEM: 675 \$·m^{-2}) [1]. d) Due to the reversed direction of ion conduction of AEMs (electro osmotic drag) compared to CEMs, the ethanol-crossover is drastically reduced in the ADEFC [6, 10].

The main challenge of ADEFC, however, is to develop a highly efficient anode catalyst for complete oxidation of ethanol to use the total chemical energy stored in ethanol molecule in electricity. Currently, there is no catalyst which cleaves the carbon–carbon bond of ethanol resulting in a CO_2 efficiency of 100% according to C1 pathway (Scheme 1) at low temperatures due to mechanistic and/or sterical effects [11].

The reaction mechanism of the ethanol oxidation on the currently used catalysts predominantly takes place on the C2 pathway (Scheme 2), resulting in various reaction intermediate deposits on

Address correspondence to Bernd Cermenek, bernd.cermenek@tugraz.at; Viktor Hacker, viktor.hacker@tugraz.at

$$CH_3CH_2OH \rightarrow CH_3CHO_{ads} \rightarrow CO_{ads}, CH_{x,ads} \rightarrow CO_2 \text{ or } CO_3^{2-}$$

Scheme 1 Alkaline ethanol electrooxidation according to C1 pathway.

$$CH_3CH_2OH \rightarrow CH_3CHO_{ads} \rightarrow CH_3CHO/CH_3COOH \text{ or } CH_3COO^-$$

Scheme 2 Alkaline ethanol electrooxidation according to C2 pathway.

the active sites of the catalyst with a decrease of its performance. The main products of alkaline EOR, generated by the reaction between adsorbed ethanol and adsorbed OH on the present catalysts, are acetic acid (CH_3COOH) and/or acetate (CH_3COO^-) [11].

The resulting reaction intermediates during the alkaline EOR deactivate easily the carbon supported Pt-based catalysts and reduce their efficiencies over time for the use in ADEFC [12–14]. Therefore, binary and ternary Pt-free catalysts are preferentially used for the alkaline EOR.

Carbon supported Pd (Pd/C) as monometallic catalyst exhibits the best performance for the alkaline EOR compared to the other noble metals e.g. Pt and Au [14, 15] and is also more cost efficient than the others [1]. The addition of oxophilic elements such as Ni, Bi, Ru, Sn, Zn or P improves the catalytic stability including tolerance to poisonous species such as CO resulting from the ethanol oxidation process (→ byproduct-tolerance) and activity (onset potential and peak current density or mass activity) of Pd catalysts with bi- and polymetallic compositions due to bifunctional, electronic and synergetic effects [2, 4, 7, 12, 16–20]. The poisoning of catalysts by reaction intermediates of the incomplete ethanol oxidation thus depends in particular on the nature of the catalyst used.

The carbon supported bismuth (Bi/C) and nickel (Ni/C) electrocatalysts display no activities to alkaline EOR in the potential useful range [2, 7, 21, 22]. A certain amount of Bi and Ni as elemental additives (oxophilic elements) however, improve the alkaline EOR performance of Pd-based catalysts considerably [7, 22, 23].

Nickel is often used as co-catalyst in Pd-based anode catalysts and promotes their alkaline EOR activities and stabilities for the ADEFC. One of many studies here, for example that of Shen and co-workers confirms the performance improvement achieved by developing and testing of Pd_xNi_y/C (C = Vulcan XC72R) catalysts with various atomic ratios. The enhancement of the alkaline EOR catalytic activities was explained due to the affinity of Ni to form Ni–OH_{ads} species which facilitate the oxidation process to CH_3COOH through a bifunctional mechanism and also by oxidative removal of poisonous ethanol species from the catalyst surface. Furthermore, the alkaline EOR performances of Pd-based electrocatalyst depend on the Ni content which leads to a decrease in alkaline EOR activity when it is too high due to the presence of Ni oxide species with low conductivity [4].

Shen et al. developed a carbon supported Pd-NiO catalyst with lower onset potential and higher current density toward the alkaline EOR compared to other Pd-oxide/C catalyst. The Pd-NiO/C anode catalyst shows higher byproduct tolerance of ethanol oxidation than Pt-based catalysts [16].

Neto et al. show the influence of Bi on the alkaline EOR performances of carbon supported binary Pd_xBi_y catalysts (Pd_xBi_y/C, C = Vulcan XC72R) with various atomic ratios of (95:05), (90:10), (80:20) and (70:30) using cyclic voltammetry for determination of their catalytic activities in comparison to a carbon supported monometallic Pd/C catalyst. The Bi content of 5 at.% and 10 at.% in Pd catalysts shifts the onset potentials toward the alkaline EOR to lower potentials in contrast with Pd/C. The PdBi/C with the atomic ratio of (95:5) exhibits the best results relating to electrocatalytic activity and stability compared to the other catalysts. This study reveals that the kinetics of alkaline EOR and the byproduct tolerance on PdBi catalysts with low Bi content are improved by the oxidative removal of adsorbed ethoxy species (rate-determining step; Scheme 2) from the catalytic sites of Pd [7].

The third element in carbon supported ternary anode catalysts for the ADEFC can additionally improve or strengthen the alkaline EOR performances of the catalyst relating to catalytic activity (onset potential and current density), long-term stability and byproduct tolerance compared to carbon supported binary EOR catalysts [9, 19, 24–35].

For example, the addition of P and Zn to carbon supported PdNi catalyst (PdNi/C, C = Vulcan XC72R), forming ternary PdNiP/C and PdNiZn/C catalysts which exhibit higher EOR activity (lower onset potential and higher peak current) than the binary PdNi/C catalyst [2, 9, 36].

Zhu et al. investigated the influence of elemental additives as Ni, Co and Ag on the electrocatalytic activities of binary PdSn-based catalysts for alkaline EOR. This study demonstrated that the PdSn-based catalyst alloyed with Ag exhibited the best results related to intrinsic activity and stability toward alkaline ethanol oxidation [19].

In this study, the influence of Ni and Bi on the alkaline EOR performance and the structure of carbon supported Pd-based nanocatalysts (Pd/C, $Pd_{60}Ni_{40}$/C, $Pd_{60}Bi_{40}$/C, $Pd_xNi_yBi_z$/C) were investigated by electrochemical and various physico-chemical methods. The optimization of the atomic composition of the novel carbon supported ternary $Pd_xNi_yBi_z$ catalyst was performed to improve its catalytic activity and stability for the alkaline EOR using the common instant reduction synthesis method with $NaBH_4$ as reducing agent for the ADEFC.

2 Experimental

2.1 Chemicals and materials

Palladium chloride ($PdCl_2$, anhydrous, 59%–60% Pd basis, Aldrich), sodium chloride (NaCl; ≥ 99.5%, Aldrich), nickel nitrate hexahydrate ($Ni(NO_3)_2{\cdot}6H_2O$, Aldrich), bismuth(III) chloride ($BiCl_3$, reagent grade, ≥ 98%, Aldrich), hydrochloric acid (HCl p.a. ≥ 32%, Fluka Analytics), Vulcan XC72R carbon black (CABOT Corporation, USA), sodium borohydride ($NaBH_4$, Sigma-Aldrich), 2-propanol (ASC ≥ 99.8%, Sigma-Aldrich), sodium hydroxide (NaOH, Aldrich), 1.0 M potassium hydroxide standard solution (KOH, FIXANAL KA 180 mL, Sigma-Aldrich), Nafion ionomer solution (5 wt.%, Quintech), ethanol abs. (99.999%, Aldrich), and ultra-pure water (≈ 18 MΩ·cm, Barnstead NANOpure Water Purification system) were used for all in this study performed experiments.

2.2 Synthesis of ternary $Pd_xNi_yBi_z$/C nanocatalysts

The carbon supported $Pd_xNi_yBi_z$ nanocatalysts were synthesized by means of the instant reduction method using $NaBH_4$ as a reducing agent [37–40]. Firstly, $PdCl_2$ and NaCl were completely dissolved in 10 mL of ultra-pure water using an ultrasonic bath for several hours. The added NaCl causes a better solubility of $PdCl_2$ in ultra-pure water due to complex formation of sodium tetrachloropalladate ($Na_2[PdCl_4]$) (Eq. (1)).

$$PdCl_2 + 2\ NaCl \rightarrow Na_2[PdCl_4] \quad (1)$$

$Ni(NO_3)_2{\cdot}6H_2O$ and $BiCl_3$ were dissolved in 10 mL of ultra-pure water. A few drops of HCl were added to the $BiCl_3$ solution to dissolve the precipitated bismuth oxychloride (BiOCl). These dissolved precursor salts were added to the $Na_2[PdCl_4]$ solution in a definite stoichiometry. Vulcan XC72R carbon black as support material was suspended in 54 mL of 2-propanol and 6 mL of ultra-pure water for 0.5 h using an ultrasonic bath. The metal salt solutions were added with additional 40 mL of ultra-pure water to suspended carbon support material (catalyst composition: 40 wt.% of metals and 60 wt.% of carbon support material). The pH of the metal salts containing solution was adjusted to 10 using 5 M NaOH. After drop-wise addition of the reducing agent solution (~ 3 eq. of $NaBH_4$(s)

in 0.6 mL of 1 M NaOH and 6 mL of ultra-pure water) to the salt suspension, the reaction mixture was vigorously stirred at 60 °C for 4 h to reduce to respective metals on carbon support material Vulcan XC72R, giving the corresponding $Pd_xNi_yBi_z$/C. After cooling of the reaction mixture to room temperature (rt), multiple washing (three times) of the catalyst suspension was performed with ultra-pure water including centrifugation at 3,500 rpm for 30 min. After each washing process, the water was decanted from the product. Finally, the obtained cleaned carbon supported $Pd_xNi_yBi_z$ nanoparticles were dried at 80 °C until constant weight was adjusted.

The syntheses of the other Pd-based nanocatalysts (Pd/C, $Pd_{60}Ni_{40}$/C and $Pd_{60}Bi_{40}$/C) were performed by the same procedure as for the development of $Pd_xNi_yBi_z$/C nanocatalysts.

2.3 Physico-chemical characterization

The actual elemental composition of each catalyst was analyzed by inductively coupled plasma optical emission spectrometry (ICP-OES). Metal concentrations of catalysts were determined by this method after microwave-assisted pressurized acid digestion. A Multiwave 3000 microwave system (Anton Paar, Graz, Austria) was used for digestion. Each material was analyzed in triplicate by digesting 5–10 mg of catalyst with 7 mL of concentrated nitric acid and 0.2 mL of $HClO_4$ (Carl Roth, Karlsruhe, Germany). Temperature was ramped to 195 °C within 15 min with the application of 1,500 W of power, followed by a dwell time of 25 min at maximum temperature. Samples were diluted to 25 mL with deionized water. The ICP-OES system was an Arcos SOP by Spectro (Kleve, Germany). Following detection wavelengths were used for each element: Bi 223.061 nm, Ni 231.604 nm, Pd 340.458 nm. Sample blanks and spikes were included in all preparation procedures.

The morphology, particle size distribution and the chemical composition (atomic ratio) of each catalyst were determined by means of the transmission electron microscopy coupled with energy dispersive X-ray spectroscopy (TEM-EDX), respectively. The images were acquired using a monochromated TF20 TEM (FEI) equipped with a Schottky field emission gun and operated at 200 kV. The EDX spectra were detected with an EDAX Si(Li) detector. For preparing the TEM grids, we followed the standard preparation procedure for powder samples by depositing a drop of alcohol suspended sample particles onto a copper TEM grid which was covered with a holey carbon support-film.

The structural composition from each synthesized catalyst was investigated with X-ray powder diffraction (XRD), using a Bruker D8-Advance diffractometer with Lynxeye detector. XRD measurements were performed from 20° to 100° 2θ, with a step size of 0.02° and a scan time of 2 s per step. Cu-Kα radiation (λ = 0.15418 nm) was used for the XRD analysis. Lattice parameters and peak-widths were calculated with Rietveld method, using PANalytical X'Pert Highscore Plus software. An estimation of mean crystallite size was performed using Scherrer-method.

The X-ray photoelectron spectroscopy (XPS) is a qualitative and quantitative method to find more information about the chemical composition from the binding energies of core-level-electrons of each contained element in synthesized catalysts. The X-ray photoelectron spectrometer works under ultrahigh-vacuum (UHV) conditions with a residual gas pressure below 10^{-10} mbar. Each catalyst sample was transferred into the analysis-chamber within several hours via load-lock. The system is also equipped with a UV-photoelectron spectrometer. The following instrumentation is used for XPS-analysis: "Multiprobe" UHV-surface-analysis system (Omicron Nanotechnology); X-ray source: DAR400 aluminium-anode; quartz-crystal monochromator XM 500; X-ray excitation energy: 1,486.70 eV (Al Kα1-line); monochromated X-ray line width (FWHM): 0.3 eV; energy analyzer: hemispherical analyzer, type EA 125 signal-detection with pulse-counting channeltron.

2.4 Electrochemical characterization

The EOR activities and stabilities of carbon supported Pd-based electrocatalysts were determined by means of cyclic voltammetry (CV) and chronoamperometry (CA) using a rotating disk electrode (RDE; Model AFE5T050GC from PINE Research Instrumentation), respectively [37, 40–42].

The electrochemical measurements were performed in an electrochemical glass cell (Metrohm) with a three-electrode-arrangement consisting of platinized titanium rod (Bank Elektronik – Intelligent controls GmbH) as counter electrode, reversible hydrogen electrode (RHE; HydroFlex®, gaskatel) as reference electrode and RDE as working electrode. A GAMRY (bi-)potentiostat (Reference 600TM Potentiostat/Galvanostat/ZRA, GAMRY Instruments Inc., Pennsylvania, USA) was used as control system. Before starting the electrochemical measurement, the RDE with glassy carbon substrate (geometric area: 0.196 cm^2) was polished using 0.05 µm alumina suspension (MasterPrep® Polishing Suspension; Buehler) and was finally rinsed with ultra-pure water.

The synthesized catalysts were dissolved in a mixture of 1.75 mL of 2-propanol, 0.737 mL of ultra-pure water and 13 µL of Nafion ionomer solution (5 wt.%, Quintech) as binder and were sonicated for 15 min in an ice-bath until a homogeneous dispersion was formed. An appropriate amount of catalyst ink was dropped onto the RDE in order to achieve the desired loading of 56 $\mu g_{Pd} \cdot cm^{-2}$. The RDE with the catalyst ink was dried by rotation to air at a rotation speed of 700 rpm for approximately 1.5 h. In the meantime, the alkaline electrolyte (1.0 M potassium hydroxide standard solution; FIXANAL KA 180 mL, Sigma-Aldrich) was purged with nitrogen gas (N_2, purity of 5.0, Air Liquide) for 30 min to remove the dissolved oxygen out of it, before the measurements were started. After that, the RDE with the respective catalyst was immersed in the 1.0 M KOH, saturated with nitrogen and CVs of each catalyst were recorded at a scan rate of 50 $mV \cdot s^{-1}$ (cleaning cycles are fast oxidation and reduction processes to remove the impurities from the surface of the catalyst) and finally at a scan rate of 10 $mV \cdot s^{-1}$ in a stationary condition, respectively. After the addition of 1.0 M ethanol (purchased from ethanol absolute, 99.999%, Aldrich) to 1.0 M KOH, further CVs of each catalyst was also recorded at a scan-rate of 10 $mV \cdot s^{-1}$ to determine the specific activity toward the ethanol oxidation in an alkaline medium.

Finally, all synthesized Pd-based catalysts were applied at a constant potential of 0.83 V for 1 h under the same operating conditions as for CV-measurements to investigate their catalytic stabilities.

3 Results and discussion

3.1 Physico-chemical characterization

An extensive physico-chemical characterization is very important for a better interpretation and understanding of performances of all synthesized nanocatalysts for the alkaline EOR. Pd-based nanocatalysts were analyzed by various methods, such as, ICP-OES, TEM-EDX, XRD and XPS in this study.

ICP-OES is an appropriate method for the quantitative determination of the elemental concentrations of the carbon supported Pd, Pd_xNi_y, Pd_xBi_y and various $Pd_xNi_yBi_z$ catalysts with the calculated atomic ratio of (100), (60:40), (60:40), and (60:20:20), (70:25:5), (70:20:10), (80:10:10), (40:20:40). Analysis results by ICP-OES are in good agreement with calculated values (= subscripts of catalysts) from the preparation of nanocatalysts (Table 1, detailed in Table S1 in the Electronic Supplementary Material (ESM)).

Metal nanoparticles (black) of the Pd/C catalyst are more evenly distributed on the carbon support material Vulcan XC72R (grey) than the bi- and ternary Pd-based catalysts. It can be observed that the presence of Bi and Ni in carbon supported Pd-based catalysts

apparently causes an agglomeration of the metal nanoparticles (Figs. 1(a)–1(d), and Figs. S1 and S2(a)–S2(d) in the ESM). It is very difficult to determine the particle size of these catalysts, because insufficient spherical particles are presented for showing reproducible results due to the agglomeration.

Table 1 Elemental analysis of Pd-based nanocatalysts by ICP-OES

Catalysts	Pd (at.%)	Ni (at.%)	Bi (at.%)
Pd/C	100	—	—
$Pd_{60}Ni_{40}/C$	60	40	—
$Pd_{60}Bi_{40}/C$	61	—	39
$Pd_{60}Ni_{20}Bi_{20}/C$	61	19	20
$Pd_{70}Ni_{25}Bi_{5}/C$	71	24	5
$Pd_{70}Ni_{20}Bi_{10}/C$	70	19	11
$Pd_{80}Ni_{10}Bi_{10}/C$	78	10	12
$Pd_{40}Ni_{20}Bi_{40}/C$	46	17	37

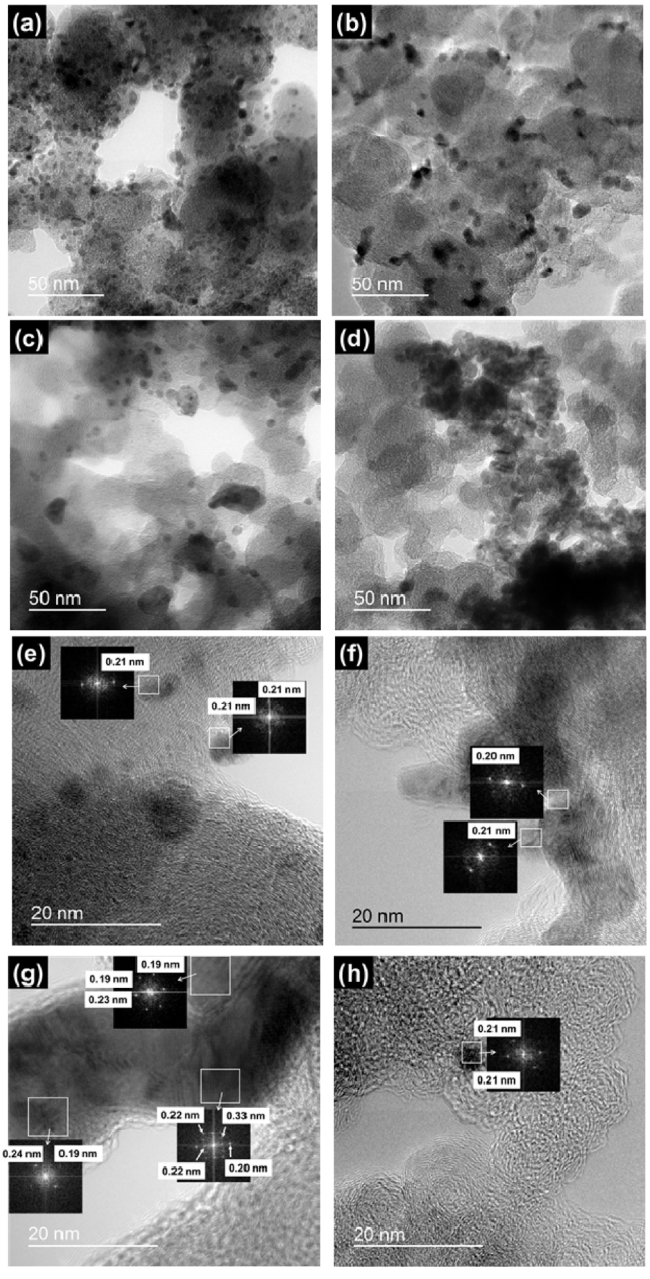

Figure 1 TEM micrographs of the (a) Pd/C, (b) $Pd_{60}Ni_{40}/C$, (c) $Pd_{60}Bi_{40}/C$ and (d) $Pd_{60}Ni_{20}Bi_{20}/C$ catalyst. HRTEM micrographs including the determined inter-planar spacing of the (e) Pd/C, (f) $Pd_{60}Ni_{40}/C$, (g) $Pd_{60}Bi_{40}/C$ and (h) $Pd_{60}Ni_{20}Bi_{20}/C$ catalyst.

Applying fast Fourier transformation (FFT) on high resolution TEM (HRTEM) micrographs show that all carbon supported Pd-based catalysts exhibit inter-planar spacing of ≈ 0.21 nm determined which complies with lattice spacing of Pd (111) (Figs. 1(e)–1(h) and Figs. S2(e)–S2(h) in the ESM). Furthermore, scanning transmission electron microscopy high-angle angular dark-field imaging (STEM-HAADF) was used to determine semi-quantitatively the metal contents of the carbon supported Pd-based catalysts at specific chosen areas by recording of EDX spectra (Figs. S3–S7 in the ESM). This analysis confirms that the metal nanoparticles of bi- and ternary Pd-based catalysts are not homogeneously distributed on the carbon support material (further details in the ESM).

The instant reduction method using $NaBH_4$ as reducing agent is therefore not the optimal catalyst synthesis method especially for controlling the homogeneous deposition of bi- and tri-metallic nanoparticles on carbon support material. Alternatively, nanocapsule, aqueous solution phase synthesis or the polyol method are other synthesis procedures to minimize the agglomeration effect for polymetallic catalysts [2, 9, 43].

The XRD patterns of all carbon supported Pd-based catalysts exhibit the typical diffraction peaks approx. at the 2θ values of 40°, 47°, 68°, 82° and 86° which can be assigned to the Pd face-centered cubic (fcc) crystalline structure (Pd_64922-ICSD) with miller indices of (111), (200), (220), (311) and (222), respectively (Fig. 2 and Fig. S8 in the ESM) [2, 4]. The diffraction peak located approx. at the 2θ value of 25° attributes to carbon black Vulcan XC72R as crystalline structure of graphite (2H)_187640-ICSD with the miller indices of (002) for all catalyst samples (Fig. 2 and Fig. S8 in the ESM) [2, 4].

The 2θ values of the binary and ternary catalysts ($Pd_{60}Ni_{40}/C$, $Pd_{60}Bi_{40}/C$, $Pd_{60}Ni_{20}Bi_{20}/C$, $Pd_{70}Ni_{20}Bi_{10}/C$ and $Pd_{40}Ni_{20}Bi_{40}/C$) are slightly lower (Tables S4–S6, S8 and S10 in the ESM) and their *d*-spacing values and lattice parameters (Table 2) are slightly higher than for the Pd/C catalyst (Table S3 in the ESM), which indicates that the Pd lattice expands and is modified by alloying with Ni and Bi. This statement is confirmed by various research groups [2, 7, 9, 12, 44, 45]. The determined inter-planar spacing for the catalysts in the recorded HRTEM micrographs (Figs. 1(e)–1(h) and Figs. S2(e)–2(h) in the ESM) conforms to the XRD results (Table 2).

Furthermore, the XRD pattern of the $Pd_{60}Ni_{40}/C$ catalyst has additional diffraction peaks approx. at 41°, 48°, 70°, 84° and 89° close to the diffraction peaks of Pd fcc crystalline structure, which is assigned to an alloying compound with a crystalline structure of $Pd_{09}Ni_{08}$_106936-ICSD with the same miller indices (Fig. 2).

The XRD patterns of $Pd_{60}Bi_{40}/C$, $Pd_{60}Ni_{20}Bi_{20}/C$, $Pd_{80}Ni_{10}Bi_{10}/C$ and $Pd_{40}Ni_{20}Bi_{40}/C$ catalysts also reveal additional diffraction peaks approx. at 24°, 30°, and 33° and were identified as crystalline structure of $Bi_2O_2(CO_3)$_252588-ICSD (Fig. 2 and Fig. S8 in the ESM).

The diffraction peak located at 27° is assigned to the crystalline structure of Bi_53797-ICSD with the miller indices of (210) for the

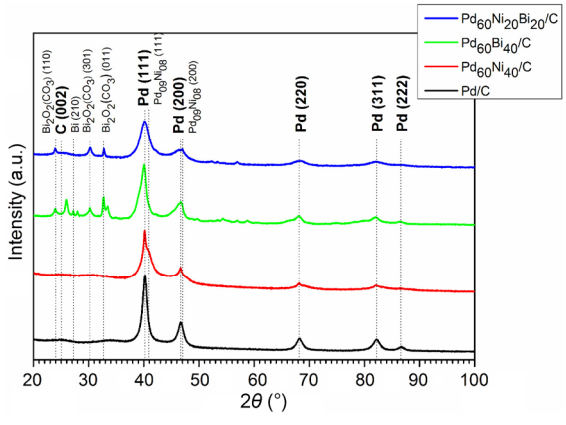

Figure 2 XRD patterns of carbon supported Pd-based nanocatalysts.

Table 2 Structure analysis of carbon supported Pd-based catalysts by XRD

Catalysts	*d*-spacing Pd (111) (nm)	Lattice parameter (nm)	Crystallite size (nm)
Pd/C	0.2244	Pd: a = 0.3891	Pd: 9
$Pd_{60}Ni_{40}/C$	0.2245	Pd: a = 0.3904 $Pd_{09}Ni_{08}$: a = 0.3816	Pd: 6–12 $Pd_{09}Ni_{08}$: 9
$Pd_{60}Bi_{40}/C$	0.2259	Pd: a = 0.3904 PdBi_tetrag: a = 0.4567; b = 0.726; c = 1.068	Pd: 9 PdBi_tetrag: 10
$Pd_{60}Ni_{20}Bi_{20}/C$	0.2247	Pd: a = 0.3894 $Bi_2O_2(CO_3)$: a = 0.385; b = 0.388; c = 1.3750	Pd: 5 $Bi_2O_2(CO_3)$: > 10
$Pd_{70}Ni_{25}Bi_5/C$	0.2230	Pd: a = 0.3863	Pd: 4
$Pd_{70}Ni_{20}Bi_{10}/C$	0.2247	Pd: a = 0.3892	Pd: 4
$Pd_{80}Ni_{10}Bi_{10}/C$	0.2229	Pd: a = 0.3894	Pd: 5
$Pd_{40}Ni_{20}Bi_{40}/C$	0.2248	Pd: a = 0.3894	Pd: 5; $Bi_2O_2(CO_3)$: 8

$Pd_{60}Bi_{40}/C$ catalyst (Fig. 2). Also, tetragonal PdBi alloy (PdBi_tetrag_56279-ICSD) is one of the main constituents of this catalyst (Table S5 in the ESM).

The XRD patterns of $Pd_{40}Ni_{20}Bi_{40}/C$ and $Pd_{60}Bi_{40}/C$ catalysts exhibit a diffraction peak approx. at 28°, which is attributed to the crystalline structure of Bi_2O_3_beta_189995-ICSD with the miller indices of (120) (Fig. S8, Tables S5 and S10 in the ESM). More details about XRD data with Rietveld-refinement for the carbon supported Pd-based catalysts are given in Tables S3–S10 in the ESM.

The crystallite sizes of Pd and the alloyed compounds in the catalysts (Pd/C, $Pd_{60}Ni_{40}/C$, $Pd_{60}Bi_{40}/C$ and $Pd_xNi_yBi_z/C$) were experimentally estimated in accordance with the Scherrer equation, assuming spherical crystallites. The crystallites are in the order of 4 to 12 nm (Table 2).

XPS was used to investigate the surface oxidation states, chemical compositions and binding energies of Pd, Ni and Bi in all synthesized catalysts. The recorded XPS spectra of Pd/C, $Pd_{60}Ni_{40}/C$, $Pd_{60}Bi_{40}/C$ and the various $Pd_xNi_yBi_z/C$ catalysts show different oxidation states for their elements (Fig. 3 and Fig. S9 in the ESM).

As expected, the XPS results relating to the atomic content determinations in the bi- and ternary carbon supported Pd-based catalysts have a discrepancy to ICP-OES analysis due to predominant overlapping of Pd and Bi on Ni at the catalyst surface leading to lower Ni content (Tables S11 and S12 in the ESM and detailed in Tables S13–S20 in the ESM: deconvolution results of the elements).

The doublets of Pd $3d_{3/2}$ and Pd $3d_{5/2}$ peaks are attributed to Pd^0 (→ metallic Pd) and Pd^{II} species (→ PdO) on the surface of all catalysts (Figs. 3(a)–3(d) and Figs. S9(a)–S9(d) in the ESM) according to Su et al., Wang et al. and Simões et al. [9, 12, 46]. It is observed that the binding energy of the $3d_{5/2}$ peak of PdO for the Ni and Bi containing Pd catalysts shifts negatively compared to Pd/C catalyst (Tables S11 and S12 in the ESM and detailed in Tables S13–S20 in the ESM). Wang et al. explain this issue by a down-shift of the d-band center of Pd i.e. the down-shift of the core-level of Pd to the Fermi level of Pd due to alloying with oxophilic elements which enhance its ethanol reaction intermediate tolerance resulting in a weak-interaction with the active sites of the catalyst (see electrochemical characterization results in Figs. 4(d), 4(h) and 4(l)) [9, 47].

Furthermore, the decrease of Pd^{II} binding energies of 335.81, 336.14, 335.95, 335.8, 335.86, 335.72 and 335.93 eV for $Pd_{60}Ni_{40}/C$, $Pd_{60}Bi_{40}/C$, $Pd_{60}Ni_{20}Bi_{20}/C$, $Pd_{75}Ni_{20}Bi_5/C$, $Pd_{70}Ni_{20}Bi_{10}/C$, $Pd_{80}Ni_{10}Bi_{10}/C$ and $Pd_{40}Ni_{20}Bi_{40}/C$ catalysts compared to the Pd^{II} binding energy of 336.27 eV for Pd/C catalyst suggests a suppression of the PdO formation due to alloying with Ni and Bi on the surface of bi- and ternary Pd-based catalysts as reported by Su et al. (Tables S11 and S12 in the ESM and detailed in Tables S13–S20 in the ESM) [12].

Figures 3(e) and 3(f) show the doublets of Ni $2p_{1/2}$ and Ni $2p_{3/2}$ which assigned to Ni^{II} species such as NiO and $Ni(OH)_2$ can be formed on the catalyst surfaces of $Pd_{60}Ni_{40}/C$ and $Pd_{60}Ni_{20}Bi_{20}/C$ according to Wang et al. [9]. The Ni 2p XPS spectra of the $Pd_{75}Ni_{20}Bi_5/C$, $Pd_{70}Ni_{20}Bi_{10}/C$, $Pd_{80}Ni_{10}Bi_{10}/C$ and $Pd_{40}Ni_{20}Bi_{40}/C$ catalysts show that in the doublets of Ni $2p_{1/2}$ and Ni $2p_{3/2}$ only one Ni^{II} species is observed which is attributable to NiO (Figs. S9(e)–S9(h) in the ESM) compared to the XPS results of the $Pd_{60}Ni_{20}Bi_{20}/C$ and $Pd_{60}Ni_{40}/C$ catalysts where $Ni(OH)_2$ as the second Ni^{II} species was identified. The measured values of the Ni 2p XPS spectra for all catalysts are undefined (Figs. 3(e) and 3(f) and Figs. S9(e)–S9(h) in the ESM)—most likely due to the inhomogeneous distribution of the metal nanoparticles on the carbon support material (see TEM-EDX results: Figs. S3–S7 in the ESM).

The surface of the $Pd_{80}Ni_{10}Bi_{10}/C$ catalyst contains the most oxide species of Pd, Ni and Bi (Tables S11, S12 and S19 in the ESM), but limits its catalytic activity for the alkaline EOR (Fig. 4(k)). The presence of the lower Ni oxide content (lower electron and proton conductivity) of the $Pd_{80}Ni_{10}Bi_{10}/C$ catalyst is the main limiting factor for its lower EOR activity compared to the other catalysts (Tables S11 and S12 in the ESM and detailed in Tables S13–S20 in the ESM). It has been shown literature that Ni oxide promotes significantly the EOR performance of the catalysts used [4, 16].

The doublets of Bi $4f_{5/2}$ and Bi $4f_{7/2}$ peaks (Fig. 3(g)) for the $Pd_{60}Bi_{40}/C$ catalyst can be attributed to Bi^0 and Bi^{III} species such as metallic

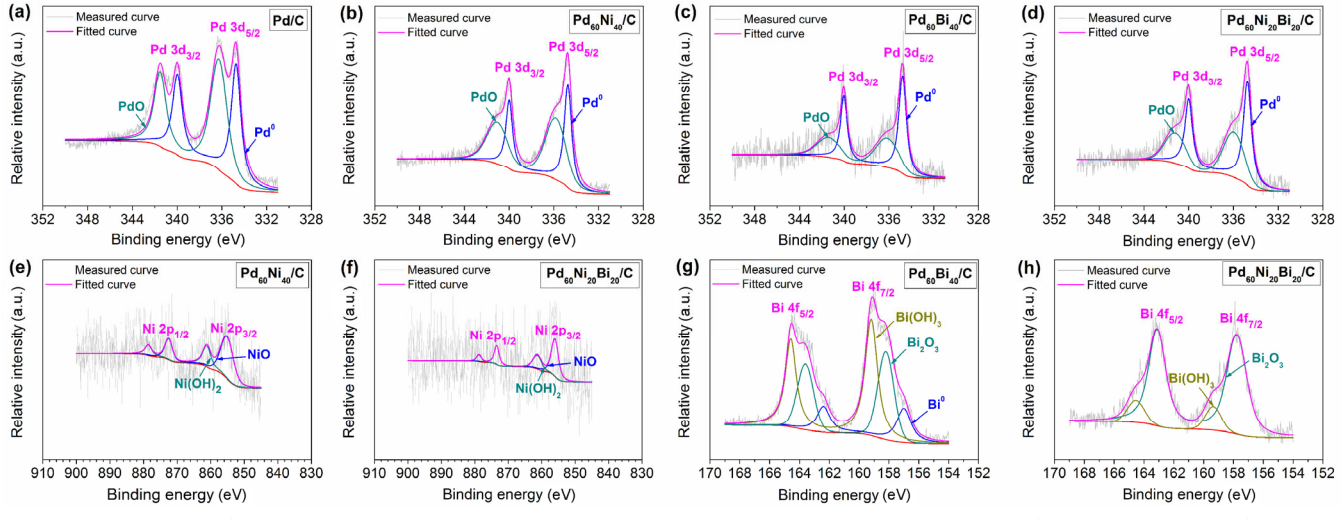

Figure 3 Pd 3d XPS spectra of the (a) Pd/C, (b) $Pd_{60}Ni_{40}/C$, (c) $Pd_{60}Bi_{40}/C$ and (d) $Pd_{60}Ni_{20}Bi_{20}/C$ catalyst. Ni 2p XPS spectra of the (e) $Pd_{60}Ni_{40}/C$ and (f) $Pd_{60}Ni_{20}Bi_{20}/C$ catalyst. Bi 4f XPS spectra of the (g) $Pd_{60}Bi_{40}/C$ and (h) $Pd_{60}Ni_{20}Bi_{20}/C$ catalyst.

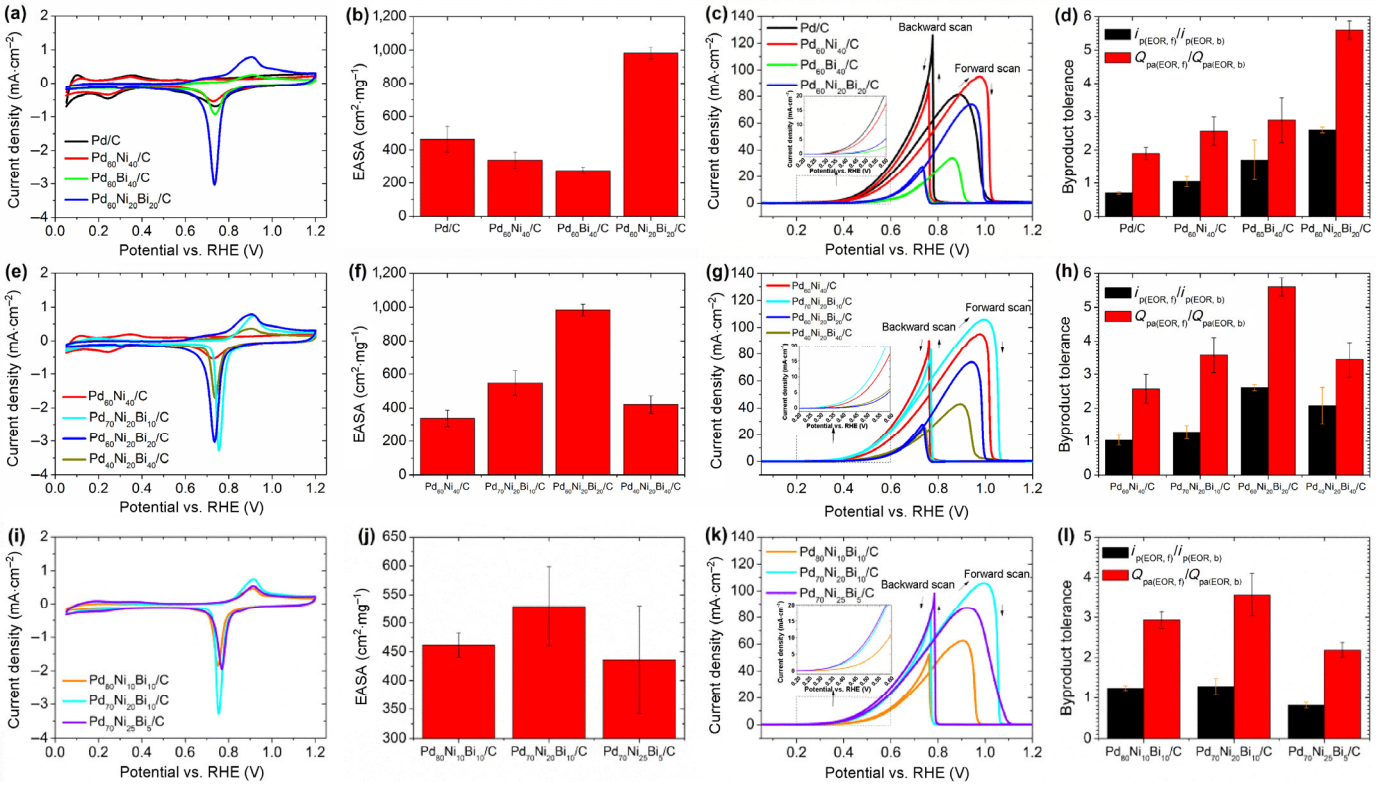

Figure 4 CVs of carbon supported Pd-based nanocatalysts (a), (e) and (i) in de-aerated 1.0 M KOH solution at 30 °C with a scan rate of 10 mV·s^{-1} and (b), (f) and (j) their resulting determined EASA; (c), (g) and (k) in a mixture of 1 M KOH and 1 M EtOH at 30 °C with a scan rate of 10 mV·s^{-1}. (d), (h) and (l) Determined tolerances of Pd-based nanocatalysts toward ethanol reaction intermediates using the EOR measurements.

Bi, Bi_2O_3 and $Bi(OH)_3$ located at 157, 158.21 and 159.19 eV [46]. Metallic Bi and Bi_2O_3 species were also identified by XRD (Table S5 in the ESM) in $Pd_{60}Bi_{40}/C$ catalyst, which confirmed the XPS results. By contrast, the doublets of Bi $4f_{5/2}$ and Bi $4f_{7/2}$ peaks (Fig. 3(h)) for the $Pd_{60}Ni_{20}Bi_{20}/C$ catalyst are attributed to Bi_2O_3 and $Bi(OH)_3$ located at 157.78 and 159.35 eV [46]. It is assumed that no complete reduction of Bi oxide species to Bi has occurred for the synthesis of the $Pd_{60}Ni_{20}Bi_{20}/C$ catalyst because the Bi peak (Bi^0) in the XPS spectrum of $Pd_{60}Ni_{20}Bi_{20}/C$ catalyst is absent (Fig. 3(h)) compared to the XPS spectrum of $Pd_{60}Bi_{40}/C$ catalyst, which conforms to the XRD results (Table S5 in the ESM).

The resulting Bi 4f XPS spectra show that metallic Bi and Bi oxide species are distributed on the surfaces of $Pd_{70}Ni_{25}Bi_5/C$, $Pd_{70}Ni_{20}Bi_{10}/C$ and $Pd_{40}Ni_{20}Bi_{40}/C$ catalysts (Figs. S9(i), S9(j), and S9(l) in the ESM). It can be observed, however, that the doublets of Bi $4f_{5/2}$ and Bi $4f_{7/2}$ peaks from the $Pd_{80}Ni_{10}Bi_{10}/C$ catalyst shift by more than 1 eV to higher binding energies, due to the increased measured oxygen content compared to the other catalysts (Figs. S9(i)–S9(k) and Tables S11, S12, S17–S20 in the ESM) and the peak of metallic Bi is absent. The explanation for the absence of Bi peak is already commented previously. An additional Bi oxide species on the $Pd_{80}Ni_{10}Bi_{10}/C$ catalyst surface, such as $Bi(OH)_3$, was identified (Fig. S9(k) in the ESM) as in $Pd_{60}Bi_{40}/C$ and $Pd_{60}Ni_{20}Bi_{20}/C$ catalysts (Figs. 3(g) and 3(h)) [46]. Furthermore, the XPS spectra obtained for C and O are demonstrated in the ESM (Figs. S10 and S11 in the ESM; additional information about XPS analysis).

Subsequently, the results of the physico-chemical characterization will be used to interpret the electrochemical characterization results of all Pd-based electrocatalysts.

3.2 Electrochemical characterization

3.2.1 *Optimum catalyst ink preparation procedure*

The catalyst ink preparation plays an important role for a homogeneous distribution on the glassy carbon substrate of RDE to obtain reproducible results for electrochemical characterization. The addition of Nafion ionomer as binder shows according to Shinozaki et al. a better quality of catalyst dispersion than is the case without Nafion ionomer in the context of the reproducibility of the electrochemical active surface area (EASA), mass activity and the specific mass activity determinations of the catalyst in RDE measurements [48]. The research group has found that the optimal dispersion of catalyst particles was obtained if the Nafion ionomer with a concentration of 24 wt.% is used. Furthermore, it was stated that the temperature of the catalyst slurry increased while sonication whereby the EASA decreased due to thermally induced degradation of smaller catalyst particles. This temperature increase can be counteracted by cooling of the catalyst slurry using an ice-water bath during the sonication process [48].

Pollet and co-workers investigated the effect of the sonication parameters used in the distribution of catalyst inks based on Pt nanoparticles with Nafion ionomer as binder [49]. The frequency and power of the sonication bath or probe significantly influence the EASA, shown in a comparison of two samples with different sonication times, the one sonicated for 120 min thus results in a EASA decline of 45% compared to the other sonicated for 30 min. It was also reported that the Nafion ionomer separated from the Pt nanoparticles which then also agglomerated and dissolved by longer sonication time [49].

The aforementioned studies concerning the effects of Nafion binder and the sonication parameters on the catalyst ink preparation and catalyst distribution on the RDE were also considered in our experiments (see Experimental Section 2.4) and improvements were implemented. In this context we have thus developed an optimum catalyst ink preparation procedure resulting in a homogeneous catalyst ink and homogeneous catalyst distribution on the RDE for reproducible results, respectively.

3.2.2 Ni and Bi effects on EOR performance of Pd/C catalysts

CVs of Pd/C, $Pd_{60}Ni_{40}$/C, $Pd_{60}Bi_{40}$/C and $Pd_{60}Ni_{20}Bi_{20}$/C catalysts were recorded stationary (without rotation) in a de-aerated 1.0 M KOH electrolyte at 30 °C in a potential range of 0.05–1.2 V (Fig. 4(a)). By the presence of Bi in carbon supported Pd electrocatalysts, the hydrogen adsorption/and absorption region (0.05–0.5 V) in the anodic scan and cathodic scan of the CVs of $Pd_{60}Bi_{40}$/C and $Pd_{60}Ni_{20}Bi_{20}$/C is drastically reduced (no distinct visible characteristic peaks) compared to the CVs of Pd/C and $Pd_{60}Ni_{40}$/C electrocatalysts (Fig. 4(a)). Neto et al. show the same effect of Bi in CVs of Pd_xBi_y/C catalysts in various atomic ratios [7]. Simões et al. confirm the suppression of the hydrogen adsorption/absorption processes by Bi on Pd and Pt containing Bi catalysts compared to monometallic Pd/C and Pt/C catalysts [46]. This suppression depends on the height of the amount of Bi atoms which are covered on the surface of the Pd catalyst and have strong interaction with Pd [46].

Furthermore, another distinctive peak in the anodic scan for the Bi containing catalysts appears at approx. 0.9 V (Fig. 4(a)), which attributed to Bi_2O_3 species from the reaction of Bi in the presence of an alkaline solution [50]. The Bi oxide species were also identified by XRD (Tables S5 and S6 in the ESM). The oxidation of Bi in KOH electrolyte starts at approx. 0.5 V to $Bi(OH)_3$ as a non-soluble compound, identified in the Bi_2O_3 phase according to Simões et al. (Fig. 4(a)) [46].

The reduction current peak in the cathodic scan between the potential of 0.5 and 0.9 V can be attributed to the formation of Pd and/or Bi oxide species in the study synthesized catalysts (Figs. 4(a), 4(e) and 4(i)) [7, 13]. By integration of the reduction peak (PdO to Pd → catalyst charge Q_{Pd}) with the Echem AnalystTM Software-Gamry, the charge was determined to calculate the EASA of each catalyst according to Eq. (2).

$$\mathrm{EASA} = \frac{Q_{\mathrm{Pd}}}{Q^{*}_{\mathrm{Pd}}}\left(\frac{1}{c_{\mathrm{L}}}\right)\left(\frac{1}{A_{\mathrm{GC}}}\right) \quad (2)$$

The calculated EASAs (incl. standard deviation) of all catalysts using the parameters (Eq. (2)) such as Q^{*}_{Pd} (= reduction charge of 405 $\mu C \cdot cm^{-2}$ of PdO to Pd, assumed value according to Jongsomjit et al. [29]), c_L (= catalyst loading of 56 $\mu g_{Pd} \cdot cm^{-2}$ on the RDE) and the A_{GC} (= surface area of 0.196 cm^2 from the glassy carbon substrate (GC) on RDE) are demonstrated in Figs. 4(b), 4(f) and 4(j) [13]. The charge of the reduction of Bi oxide to Bi could not be considered for the EASA calculation of the Bi containing catalysts because the Bi oxide reduction arises in the same potential range as the Pd oxide reduction. Therefore, the excellent EASA result of the $Pd_{60}Ni_{20}Bi_{20}$/C catalyst compared to the other carbon supported Pd-based electrocatalysts (Fig. 4(b) and Table 3) is only comparable with the $Pd_{60}Bi_{40}$/C catalysts. The $Pd_{60}Ni_{20}Bi_{20}$/C catalyst with a 2.6-fold higher EASA than the $Pd_{60}Bi_{40}$/C catalyst depends on the Bi content. Neto et al. report that the increased addition of Bi to Pd catalysts causes more agglomerations whereby the active sites of Pd are blocked resulting in decreasing of the EASA (Fig. 4(b)) and consequently the catalytic activity (Fig. 4(c)) [7].

Additionally, $Pd_{60}Ni_{40}$/C and $Pd_{60}Ni_{20}Bi_{20}$/C catalysts were investigated under the same measurement conditions in Fig. S12(a) in the ESM, but using the potential range of 0.05–1.5 V to find out if Ni is present in the catalysts. Figure S12(b) in the ESM shows that the peak in the anodic scan at the potential range of 1.3–1.5 V as the oxidation of $Ni(OH)_2$ to NiOOH whereas the peak in the cathodic scan at the potential range of 1.2–1.4 V as the reduction of NiOOH to $Ni(OH)_2$ are represented for both catalysts $Pd_{60}Ni_{40}$/C and $Pd_{60}Ni_{20}Bi_{20}$/C according to Zhang et al. [2]. It is evident and also as expected that the current density of the Ni oxidation and reduction peaks of $Pd_{60}Ni_{40}$/C catalyst are higher than for the $Pd_{60}Ni_{20}Bi_{20}$/C catalyst (Fig. S12 in the ESM).

The determination of the catalytic activity and stability toward EOR of Pd/C, $Pd_{60}Ni_{40}$/C, $Pd_{60}Bi_{40}$/C and $Pd_{60}Ni_{20}Bi_{20}$/C catalysts takes place in a mixture of 1 M KOH and 1 M EtOH by means of CV using RDE (without rotation) at 30 °C. The $Pd_{60}Ni_{40}$/C catalyst exhibits the best result relating to EOR activity compared to the other carbon supported Pd-based catalysts (Fig. 4(c) and Table 3).

Nickel as an additive is more oxophilic than Bi in the resulting low onset potential of $Pd_{60}Ni_{40}$/C catalyst with a high produced current density toward ethanol oxidation in alkaline medium compared to catalysts containing Bi (see small figure in Fig. 4(c) and Table 3) [51]. This means that Ni generates more adsorbed OH on the Pd catalyst surface than Bi to oxidize the adsorbed ethanol species quickly. Zhang et al. report that onset potentials of Pd_xNi_y/C based catalysts toward ethanol oxidation depend significantly on the surface concentration of Ni [2].

Furthermore, in the synthesized Pd-based electrocatalysts Bi facilitates an essential improvement of the tolerance toward ethanol intermediates from the EOR in the electrolyte mixture of 1 M KOH and 1 M EtOH (Fig. 4(d) and Table 3), but their onset potentials shift to higher potentials (see small figure in Fig. 4(c) and Table 3) and their catalytic activities decrease (Fig. 4(c) and Table 3) compared to Pd/C and $Pd_{60}Ni_{40}$/C catalysts, respectively. The higher onset potential and the lower specific activity of the $Pd_{60}Bi_{40}$/C catalyst toward the ethanol oxidation compared to the $Pd_{60}Ni_{20}Bi_{20}$/C catalyst (Fig. 4(c) and Table 3) are due to its higher Bi content thus formed Bi oxide species block multiple active sites of Pd [7].

The tolerance toward EOR intermediates was determined by two different methods (Figs. 4(d), 4(h) and 4(l)): 1) using the ratio of the peak current density of the forward ($i_{p(EOR,f)}$) and backward scan ($i_{p(EOR,b)}$) [12], and 2) using the ratio of the integrated oxidation peak current density area (total charge) of forward ($Q_{pa(EOR,f)}$) and backward scan ($Q_{pa(EOR,b)}$) from EOR measurements in alkaline medium (Figs. 4(c), 4(g) and 4(k)), respectively [51]. Sekol et al. identified the second method as being a more accurate method than the first one for determining the catalyst tolerance toward reaction intermediates resulting from the EOR [51]. The higher the value the better is the tolerance of the catalyst toward the reaction intermediates of ethanol. This means that the ethanol reaction intermediates or poisonous species which are not oxidized in the forward scan, are oxidatively removed in the backward scan [12, 51].

Figure 4(d) shows that the $Pd_{60}Ni_{20}Bi_{20}$/C catalyst exhibits the best tolerance by far toward the reaction intermediates of ethanol compared to the other catalysts. The excellent results relating to the byproduct tolerance of the Bi containing catalysts can be explained by the study of Paschos et al. [52]. In a CO stripping test was stated that one Bi adatom blocked three Pd surface atoms for avoiding the poisoning of the Pd active sites in the BiPd-based catalyst [52].

It should be noted, the i_f/i_b or Q_f/Q_b ratio is not a sufficient but a necessary indicator for evaluation of anti-poisoning tolerance of a catalyst as it has been discussed in Refs. [53, 54].

After the Pd/C, $Pd_{60}Ni_{40}$/C, $Pd_{60}Bi_{40}$/C and $Pd_{60}Ni_{20}Bi_{20}$/C nanocatalysts were subjected to 1 h stress at an applied potential of 0.83 V, the novel $Pd_{60}Ni_{20}Bi_{20}$/C catalyst showed the best result in terms of electrocatalytic stability toward alkaline EOR (Fig. 5(a) and Table 3). The order of the decrease of produced current density in percentage of all catalysts from the start until to the end of CA measurement is given in Fig. 5(b). The decrease of current densities of all catalysts after 1 h stress is listed in following order: $Pd_{60}Bi_{40}$/C > $Pd_{60}Ni_{40}$/C > Pd/C > $Pd_{60}Ni_{20}Bi_{20}$/C.

3.2.3 Varying atomic ratios of Pd, Ni and Bi in EOR catalysts

Furthermore, the electrocatalytic activities and stabilities of the synthesized carbon supported $Pd_xNi_yBi_z$ catalysts ($Pd_{70}Ni_{25}Bi_5$/C, $Pd_{70}Ni_{20}Bi_{10}$/C, $Pd_{80}Ni_{10}Bi_{10}$/C, $Pd_{40}Ni_{20}Bi_{40}$/C) were characterized by CV and CA using the RDE in static mode with metal loading

of 56 $\mu g_{Pd} \cdot cm^{-2}$ under same operating conditions (Figs. 4(e)–4(l)) as for Pd/C, $Pd_{60}Ni_{40}$/C, $Pd_{60}Bi_{40}$/C and $Pd_{60}Ni_{20}Bi_{20}$/C catalysts.

The influence of varied Bi content on the EOR performances of the synthesized catalysts $Pd_{40}Ni_{20}Bi_{40}$/C and $Pd_{70}Ni_{20}Bi_{10}$/C were investigated and compared to the benchmarks $Pd_{60}Ni_{40}$/C and $Pd_{60}Ni_{20}Bi_{20}$/C (Figs. 4(e)–4(h)) which possessed the best catalytic performances in terms of alkaline EOR activity and stability (byproduct tolerance), respectively (Figs. 4(c)and 4(d)).

The recorded CV of the $Pd_{70}Ni_{20}Bi_{10}$/C catalyst in de-aerated 1.0 M KOH shows a peak in the potential region between 0.1 and 0.2 V indicating an occurring hydrogen sorption reaction (Fig. 4(e)). It was confirmed that $Pd_xNi_yBi_z$/C catalysts with more than 10 at.% of Bi ($Pd_{60}Ni_{20}Bi_{20}$/C and $Pd_{40}Ni_{20}Bi_{40}$/C) lead to a suppression of the hydrogen adsorption and the absorption process itself compared to the CVs of $Pd_{60}Ni_{40}$/C and $Pd_{70}Ni_{20}Bi_{10}$/C catalysts (Fig. 4(e)). This effect was observed by adding a specific quantity of Bi to Pd as well as to Pt-based catalysts [7, 21, 46]. Neto et al. improved the alkaline EOR activities of carbon supported Pd catalysts by adding of decreased Bi contents [7], whereupon the Pt_xBi_y based catalysts were enhanced by increasing of Bi contents [21].

Further distinctive peaks in the potential regions of the anodic scan between 0.8 and 1.0 V and of the cathodic scan between 0.5 and 0.9 V are attributed to the oxidized and reduced Bi and Pd species, respectively (Fig. 4(e)). From the obtained XPS and XRD data we suggest that the peak around 0.9 V in the anodic scan (Figs. 4(e) and 4(i)) mainly originates from the oxidation of Bi and Bi oxide species. Simões et al. observed that this characteristic peak became higher in the CVs of carbon supported binary Pd_xBi_y catalysts by increasing of Bi content [46].

The former statement does not coincide with our RDE-CV measurements because this peak of $Pd_{40}Ni_{20}Bi_{40}$/C is lower than for $Pd_{60}Ni_{20}Bi_{20}$/C catalyst (Fig. 4(e)). Here, many cleaning cycles (= recorded CVs at a scan rate of 50 $mV \cdot s^{-1}$) of the $Pd_{40}Ni_{20}Bi_{40}$/C catalyst had to be conducted until a stable CV was obtained, because the peak, which was assigned to Bi oxide species, decreased with increased cycles. This decreased trend can be thus explained by the presence of impurities which undergo an oxidative removal or other species that are dissolved with increasing potential. As this phenomenon was also observed in the RDE-CV measurements of the $Pd_{60}Bi_{40}$/C catalyst. It is assumed that Bi^0-agglomerates, mentioned by Simões et al., are oxidized and dissolved into the electrolyte [46].

Our studies are supported by the observation that the current densities in the EOR measurements of $Pd_{60}Bi_{40}$/C and $Pd_{40}Ni_{20}Bi_{40}$/C catalysts increased when more cycles were performed. The proven Bi^0-agglomerates in the $Pd_{60}Bi_{40}$/C which block the active sites of Pd are gradually dissolved and lead to higher activities after multiple CV cycles and it is assumed that this is also valid for the $Pd_{40}Ni_{20}Bi_{40}$/C catalyst.

The study of Simões et al. reported that Bi^0 agglomerates in catalysts with a Bi content as high as 20% or higher by EDX analysis. However, the agglomerations were not identified in carbon supported Pd_xBi_y catalysts with Bi content lower than 20% [46]. The prior statement cannot be confirmed by our TEM results (Figs. 1(c) and 1(d), and Figs. S1(c)–S1(h) and S2(a)–S2(d) in the ESM).

The $Pd_{60}Ni_{20}Bi_{20}$/C catalyst as benchmark exhibits the highest EASA among all in this study synthesized carbon supported $Pd_xNi_yBi_z$ catalysts, followed by $Pd_{70}Ni_{20}Bi_{10}$/C catalyst (Table 3 and Fig. 4(f)). These results are conclusive in respect to the findings of Simões et al., that the reduction peak approx. at 0.75 V not only originates from Pd oxide species alone but also that other oxidized species are reduced in this region [46]. As more Bi is incorporated in the $Pd_{60}Ni_{20}Bi_{20}$/C catalyst and more Bi species can be oxidized, the reduction peak approx. at 0.75 V in the cathodic sweep is also more distinct compared to $Pd_{70}Ni_{20}Bi_{10}$/C catalyst (Fig. 4(e)).

The EASA of the $Pd_{40}Ni_{20}Bi_{40}$/C is assumed to be lower due to the low Pd content and the high Bi content leading to agglomerations. The $Pd_{70}Ni_{20}Bi_{10}$/C catalyst exceeded the alkaline EOR performance of $Pd_{60}Ni_{40}$/C in terms of peak current density and onset potential (Fig. 4(g) and Table 3). The onset potential for the alkaline EOR was decreased by 54 mV using the $Pd_{70}Ni_{20}Bi_{10}$/C and the peak current density could be increased by 10 $mA \cdot cm^{-2}$ compared to $Pd_{60}Ni_{40}$/C (Fig. 4(g) and Table 3). This result proves that small amounts of Bi in the carbon supported $Pd_xNi_yBi_z$ catalyst enhance the activity and kinetics toward the EOR in an alkaline medium.

Even though $Pd_{70}Ni_{20}Bi_{10}$/C catalyst shows the best results in respect to the onset potential and peak current density toward alkaline EOR (Table 3), the byproduct tolerance is not as good as for $Pd_{60}Ni_{20}Bi_{20}$/C catalyst. However, $Pd_{70}Ni_{20}Bi_{10}$/C is the second best catalyst among all of those tested if the total current for the calculation of the byproduct tolerance is used (Fig. 4(h) and Table 3). An explanation for this result could be that in the $Pd_{60}Ni_{20}Bi_{20}$/C catalyst containing 20 at.% of Bi, more Pd active sites are protected by Bi atoms. However, the reactant is hindered from reaching the active sites leading to lower activity and higher stability than $Pd_{70}Ni_{20}Bi_{10}$/C catalyst. By contrast, in the $Pd_{70}Ni_{20}Bi_{10}$/C catalyst only 10 at.% of Bi protects the active sites of Pd from poisoning resulting in a lower byproduct tolerance than for $Pd_{60}Ni_{20}Bi_{20}$/C catalyst. However, the active sites are better accessible for ethanol and a higher EOR activity is observed in an alkaline medium (Fig. 4(h)).

The CA results of $Pd_{70}Ni_{20}Bi_{10}$/C catalyst (Fig. 5(c)) correlate with the results obtained from the byproduct tolerance determinations (Fig. 4(h)). The $Pd_{60}Ni_{20}Bi_{20}$/C catalyst, which exhibits the highest byproduct tolerance was also found to be the most stable one in the CA measurement followed by $Pd_{70}Ni_{20}Bi_{10}$/C, which still had almost 40% of the starting current density after 1 h at an applied potential of 0.83 V (Fig. 5(d) and Table 3).

Since the previous studies on the influence of Ni and Bi in carbon supported ternary $Pd_xNi_yBi_z$ catalysts have shown that a low Bi content enhances the alkaline EOR activity of the catalyst, the attempt was

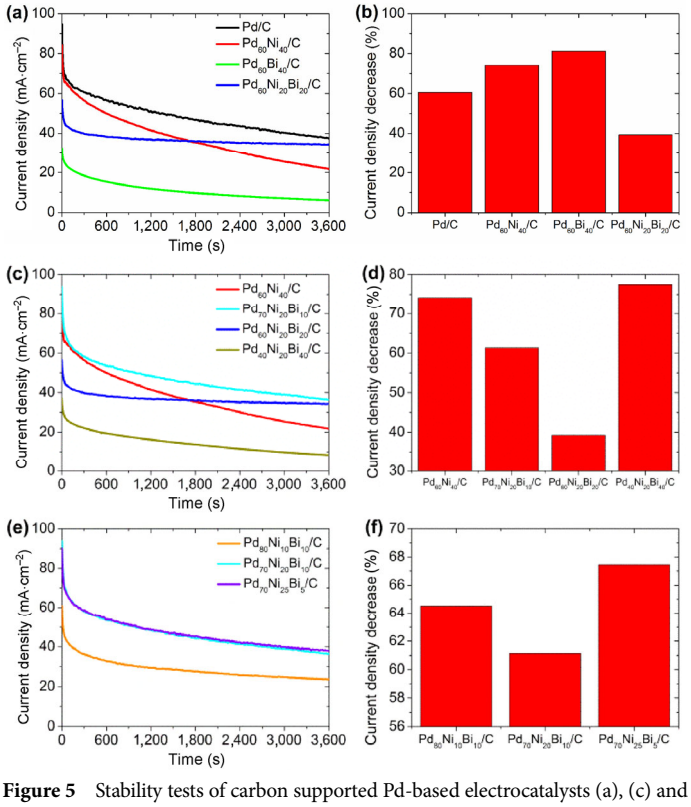

Figure 5 Stability tests of carbon supported Pd-based electrocatalysts (a), (c) and (e) in a mixture of 1 M KOH and 1 M EtOH at an applied potential of 0.83 V for 3,600 s using the CA method and (b), (d) and (f) their resulting current density decrease, given in percentage.

Table 3 Electrochemical characterization results of all carbon supported Pd-based electrocatalysts

Catalysts	EASA[a] ($cm^2 \cdot mg^{-1}$)	i_f[b] ($mA \cdot cm^{-2}$)	i_b[b] ($mA \cdot cm^{-2}$)	i_f/i_b[c]	$Q_{pa,f}/Q_{pa,b}$[d]	E_{onset}[e] (V)	i_{Start}[f] ($mA \cdot cm^{-2}$)	i_{End}[f] ($mA \cdot cm^{-2}$)	i_D[g] (%)
Pd/C	463 ± 78	81.17	125.95	0.70 ± 0.04	1.90 ± 0.18	0.280 ± 0.015	94.97	37.37	61
$Pd_{60}Ni_{40}/C$	339 ± 49	95.11	90.05	1.04 ± 0.15	2.57 ± 0.42	0.290 ± 0.018	84.14	21.77	74
$Pd_{60}Bi_{40}/C$	276 ± 22	34.03	14.96	1.70 ± 0.60	2.89 ± 0.67	0.352 ± 0.015	32.16	6.02	81
$Pd_{60}Ni_{20}Bi_{20}/C$	983 ± 35	73.93	27.60	2.60 ± 0.09	5.60 ± 0.27	0.348 ± 0.007	56.59	34.39	39
$Pd_{70}Ni_{25}Bi_5/C$	436 ± 94	87.28	98.19	0.81 ± 0.07	2.19 ± 0.18	0.239 ± 0.009	90.01	37.88	58
$Pd_{70}Ni_{20}Bi_{10}/C$	549 ± 72	105.77	83.39	1.28 ± 0.20	3.57 ± 0.53	0.236 ± 0.005	93.88	36.34	61
$Pd_{80}Ni_{10}Bi_{10}/C$	462 ± 21	62.55	52.30	1.24 ± 0.06	2.93 ± 0.53	0.274 ± 0.008	60.87	23.67	61
$Pd_{40}Ni_{20}Bi_{40}/C$	421 ± 52	42.79	25.37	2.07 ± 0.54	3.43 ± 0.52	0.323 ± 0.033	37.14	8.36	77

[a]Electrochemical active surface area (EASA) determination; [b]i_f and i_b: peak current density of forward and backward scan; [c]i_f/i_b: byproduct tolerance using peak current density of forward and backward scan; [d]$Q_{pa,f}/Q_{pa,b}$: byproduct tolerance using the charge of the integrated peak current density area of the forward and backward scan; [e]E_{onset}: onset potential of the ethanol oxidation; [f]i_{Start} and i_{End}: resulting current densities at an applied potential of 0.83 V after 0 s and 3,600 s; [g]i_D: loss of current density after stress test at an applied of 0.83 V for 3,600 s.

made to decrease the Bi content even further than 10 at.% to 5 at.%. Additionally, the Pd content was increased to test whether the alkaline EOR activity would rise further with a higher Pd content. The catalysts $Pd_{70}Ni_{25}Bi_5/C$ and $Pd_{80}Ni_{10}Bi_{10}/C$ were therefore synthesized, electrochemically characterized and the obtained results were compared with $Pd_{70}Ni_{20}Bi_{10}/C$ catalyst (Figs. 4(i)–4(l), 5(e) and 5(f)).

In the EOR measurements, the $Pd_{70}Ni_{25}Bi_5/C$ and $Pd_{80}Ni_{10}Bi_{10}/C$ catalysts could not exceed the peak current density of the $Pd_{70}Ni_{20}Bi_{10}/C$ catalyst (Fig. 4(k)). However, $Pd_{70}Ni_{25}Bi_5/C$ has a low onset potential (0.239 V), very close to that of $Pd_{70}Ni_{20}Bi_{10}/C$ (0.236 V) (see small figure in Fig. 4(k) and Table 3). This supports the study that low amounts of Bi enhance the kinetics at the anode for the EOR in alkaline medium but the increase in peak current density could not be confirmed. The onset potential and the peak current density of the $Pd_{80}Ni_{10}Bi_{10}/C$ catalyst were both reduced compared to $Pd_{70}Ni_{20}Bi_{10}/C$ (Fig. 4(k)). This result is also conclusive when taking into account that the Ni content was reduced and the addition of higher amounts of Ni are necessary for a catalyst with high activity [2].

As expected, the byproduct tolerance of $Pd_{70}Ni_{25}Bi_5/C$ decreases when the Bi content is reduced from 10 at.% to 5 at.%. Also for the $Pd_{80}Ni_{10}Bi_{10}/C$ catalyst the byproduct tolerance is lower compared to $Pd_{70}Ni_{20}Bi_{10}/C$ but still higher than for $Pd_{70}Ni_{25}Bi_5/C$ (Fig. 4(l) and Table 3).

The CVs of the $Pd_{70}Ni_{25}Bi_5/C$, $Pd_{80}Ni_{10}Bi_{10}/C$ and $Pd_{70}Ni_{20}Bi_{10}/C$ catalysts exhibit similar curve progressions in 1.0 M KOH solution (Fig. 4(i)). The EASAs of $Pd_{70}Ni_{25}Bi_5/C$ and $Pd_{80}Ni_{10}Bi_{10}/C$ catalysts are lower than the EASA of $Pd_{70}Ni_{20}Bi_{10}/C$ (Fig. 4(j) and Table 3). The $Pd_{70}Ni_{25}Bi_5/C$ and $Pd_{80}Ni_{10}Bi_{10}/C$ catalysts also show lower stability than $Pd_{70}Ni_{20}Bi_{10}/C$ in the CA measurements (Figs. 5(e) and 5(f) and Table 3). However, the results are still better than for $Pd_{60}Ni_{40}/C$ (Table 3) showing the positive effect of Bi on the stability toward alkaline EOR.

3.2.4 *$Pd_{70}Ni_{20}Bi_{10}/C$ as promising EOR catalyst*

It can be concluded that higher amounts of Ni in Pd-based anode catalysts for the alkaline DEFC enhance the activity for the EOR. In case of Bi, it is confirmed that lower amounts of Bi enhance the activity and kinetics at the anode for the EOR in an alkaline medium. This was observed as a low onset potential and high peak current density for catalysts with low Bi concentration. It was also found that a higher concentration of Bi (20 at.%) improves the byproduct tolerance and the stability of the catalyst.

The $Pd_{70}Ni_{20}Bi_{10}/C$ catalyst is the most active catalyst toward alkaline EOR among all tested catalysts (Figs. 4(g) and 4(k)) and exhibits the second best results in terms of byproduct tolerance (Table 3). The maximum current density of 106 $mA \cdot cm^{-2}$ (mass activity: 1,889 $mA \cdot mg^{-1}$—relating to Pd loading) from the novel ternary $Pd_{70}Ni_{20}Bi_{10}/C$ catalyst is, despite agglomerations, an outstanding value for the alkaline EOR compared to Ref. [55] as well as to Table S21 in the ESM. Considerably higher maximum current densities of the ternary $Pd_{70}Ni_{20}Bi_{10}/C$ catalyst could be achieved under the CV measurement conditions (e.g. with a scan rate of 50 $mV \cdot s^{-1}$ instead of 10 $mV \cdot s^{-1}$) applied in Ref. [55] and Table S21 in the ESM.

The electrochemical characterization results of all carbon supported Pd-based nanocatalysts are summarized in Table 3. Further details about the effects of the Pd, Ni and Bi species/ions on the catalytic properties and surface structures are discussed in the ESM.

4 Conclusions

Carbon supported Pd-based nanocatalysts (Pd/C, $Pd_{60}Ni_{40}/C$, $Pd_{60}Bi_{40}/C$ and $Pd_xNi_yBi_z/C$) were successfully developed using the instant reduction synthesis method with $NaBH_4$ as reducing agent, comprehensively characterized and the influence of the admetals Ni and Bi in the carbon supported binary and ternary Pd-based EOR catalysts was determined.

The alkaline EOR performance (catalytic activity, byproduct tolerance, and stability) of the novel carbon supported ternary $Pd_xNi_yBi_z$ catalyst was optimized by varying the atomic ratios of Pd, Ni and Bi for the application in alkaline direct ethanol fuel cells. The carbon supported Pd:Ni:Bi catalyst with the atomic ratio of 70:20:10 exhibits the highest catalytic activity compared to the other synthesized $Pd_xNi_yBi_z/C$ catalysts as well as to the benchmarks Pd/C, $Pd_{60}Ni_{40}/C$ and $Pd_{60}Bi_{40}/C$. The maximum onset potential reduction of 116 mV and the peak current density enhancement of 71 $mA \cdot cm^{-2}$ were achieved for the alkaline EOR on the $Pd_{70}Ni_{20}Bi_{10}/C$ catalyst.

The low Bi content (≤ 10 at.%) in the synthesized ternary $Pd_xNi_yBi_z$ catalysts promotes the alkaline EOR kinetics leading to high current densities and low onset potentials, whereas the use of high amounts of Bi (> 20 at.%) blocks the active sites of the used catalysts resulting in a decrease of the EOR activities.

For further improvement of the EOR performance of the $Pd_{70}Ni_{20}Bi_{10}/C$ catalyst, the substitution of the support material and alternative deposition methods for spherical metal nanoparticles with defined particle size and low tendency to agglomeration are investigated.

Acknowledgements

Financial support from the Austrian Climate Energy Fund, Austrian Federal Ministry of Transport, Innovation and Technology (BMVIT), The Austrian Research Promotion Agency (FFG) through the program "Energy Mission Austria" and the IEA research cooperation are gratefully acknowledged. We thank Dr. Christian Palfinger for performing of the XPS analysis.

Funding: Open access funding provided by Graz University of Technology

Electronic Supplementary Material: Supplementary material (further details of the ICP-OES, TEM-EDX, XRD, XPS and CV measurements) is available in the online version of this article at https://doi.org/10.1007/s12274-019-2277-z.

References

[1] An, L.; Zhao, T. S.; Li, Y. S. Carbon-neutral sustainable energy technology: Direct ethanol fuel cells. *Renew. Sustain. Energy Rev.* **2015**, *50*, 1462–1468.

[2] Zhang, Z. Y.; Xin, L.; Sun, K.; Li, W. Z. Pd-Ni electrocatalysts for efficient ethanol oxidation reaction in alkaline electrolyte. *Int. J. Hydrogen Energy* **2011**, *36*, 12686–12697.

[3] Shen, S. Y.; Zhao, T. S.; Wu, Q. X. Product analysis of the ethanol oxidation reaction on palladium-based catalysts in an anion-exchange membrane fuel cell environment. *Int. J. Hydrogen Energy* **2012**, *37*, 575–582.

[4] Shen, S. Y.; Zhao, T. S.; Xu, J. B.; Li, Y. S. Synthesis of PdNi catalysts for the oxidation of ethanol in alkaline direct ethanol fuel cells. *J. Power Sources* **2010**, *195*, 1001–1006.

[5] Zhao, T. S.; Li, Y. S.; Shen, S. Y. Anion-exchange membrane direct ethanol fuel cells: Status and perspective. *Front. Energy Power Eng. China* **2010**, *4*, 443–458.

[6] An, L.; Zhao, T. S. Transport phenomena in alkaline direct ethanol fuel cells for sustainable energy production. *J. Power Sources* **2017**, *341*, 199–211.

[7] Neto, A. O.; Tusi, M. M.; de Oliveira Polanco, N. S.; da Silva, S. G.; Santos, M. C.; Spinacé, E. V. PdBi/C electrocatalysts for ethanol electro-oxidation in alkaline medium. *Int. J. Hydrogen Energy* **2011**, *36*, 10522–10526.

[8] Wu, Q. M.; Jiang, L. H.; Qi, L. T.; Yuan, L. Z.; Wang, E. D.; Sun, G. Q. Electrocatalytic activity and stability of Ag-MnO_x/C composites toward oxygen reduction reaction in alkaline solution. *Electrochim. Acta* **2014**, *123*, 167–175.

[9] Wang, Y.; Shi, F. F.; Yang, Y. Y.; Cai, W. B. Carbon supported Pd-Ni-P nanoalloy as an efficient catalyst for ethanol electro-oxidation in alkaline media. *J. Power Sources* **2013**, *243*, 369–373.

[10] Yu, E. H.; Wang, X.; Krewer, U.; Li, L.; Scott, K. Direct oxidation alkaline fuel cells: From materials to systems. *Energy Environ. Sci.* **2012**, *5*, 5668–5680.

[11] Kamarudin, M. Z. F.; Kamarudin, S. K.; Masdar, M. S.; Daud, W. R. W. Review: Direct ethanol fuel cells. *Int. J. Hydrogen Energy* **2013**, *38*, 9438–9453.

[12] Su, P. C.; Chen, H. S.; Chen, T. Y.; Liu, C. W.; Lee C. H.; Lee, J. F.; Chan, T. S.; Wang, K. W. Enhancement of electrochemical properties of Pd/C catalysts toward ethanol oxidation reaction in alkaline solution through Ni and Au alloying. *Int. J. Hydrogen Energy* **2013**, *38*, 4474–4482.

[13] Singh, R. N.; Anindita, A. S. Electrocatalytic activity of binary and ternary composite films of Pd, MWCNT, and Ni for ethanol electro-oxidation in alkaline solutions. *Carbon* **2009**, *47*, 271–278.

[14] Ma, L.; Chu, D.; Chen, R. R. Comparison of ethanol electro-oxidation on Pt/C and Pd/C catalysts in alkaline media. *Int. J. Hydrogen Energy* **2012**, *37*, 11185–11194.

[15] Geraldes, A. N.; da Silva, D. F.; Pino, E. S.; da Silva, J. C. M.; de Souza, R. F. B.; Hammer, P.; Spinacé, E. V.; Neto, A. O.; Linardi, M.; dos Santos, M. C. Ethanol electro-oxidation in an alkaline medium using Pd/C, Au/C and PdAu/C electrocatalysts prepared by electron beam irradiation. *Electrochim. Acta* **2013**, *111*, 455–465.

[16] Shen, P. K.; Xu, C. W. Alcohol oxidation on nanocrystalline oxide Pd/C promoted electrocatalysts. *Electrochem. Commun.* **2006**, *8*, 184–188.

[17] Ma, L.; He, H.; Hsu, A.; Chen, R. R. PdRu/C catalysts for ethanol oxidation in anion-exchange membrane direct ethanol fuel cells. *J. Power Sources* **2013**, *241*, 696–702.

[18] Liang, Z. X.; Zhao, T. S.; Xu, J. B.; Zhu, L. D. Mechanism study of the ethanol oxidation reaction on palladium in alkaline media. *Electrochim. Acta* **2009**, *54*, 2203–2208.

[19] Zhu, F. C.; Wang, M.; He, Y. W.; Ma, G. S.; Zhang, Z. H.; Wang, X. G. A comparative study of elemental additives (Ni, Co and Ag) on electrocatalytic activity improvement of PdSn-based catalysts for ethanol and formic acid electro-oxidation. *Electrochim. Acta* **2014**, *148*, 291–301.

[20] Moraes, L. P. R.; Matos, B. R.; Radtke, C.; Santiago, E. I.; Fonseca, F. C.; Amico, S. C.; Malfatti, C. F. Synthesis and performance of palladium-based electrocatalysts in alkaline direct ethanol fuel cell. *Int. J. Hydrogen Energy* **2016**, *41*, 6457–6468.

[21] Tusi, M. M.; Polanco, N. S. O.; da Silva, S. G.; Spinacé, E. V.; Neto, A. O. The high activity of PtBi/C electrocatalysts for ethanol electro-oxidation in alkaline medium. *Electrochem. Commun.* **2011**, *13*, 143–146.

[22] Nikiforova, T. G.; Datskevich, O. A.; Maleev, V. V. Palladium catalysts on porous nickel substrates for alcohol fuel cells. *Russ. J. Appl. Chem.* **2012**, *85*, 1871–1878.

[23] Yang, H. J.; Wang, H.; Li, H.; Ji, S.; Davids, M. W.; Wang, R. F. Effect of stabilizers on the synthesis of palladium-nickel nanoparticles supported on carbon for ethanol oxidation in alkaline medium. *J. Power Sources* **2014**, *260*, 12–18.

[24] Modibedi, R. M.; Masombuka, T.; Mathe, M. K. Carbon supported Pd–Sn and Pd–Ru–Sn nanocatalysts for ethanol electro-oxidation in alkaline medium. *Int. J. Hydrogen Energy* **2011**, *36*, 4664–4672.

[25] Shen, S. Y.; Zhao, T. S.; Xu, J. B.; Li, Y. S. High performance of a carbon supported ternary PdIrNi catalyst for ethanol electro-oxidation in anion-exchange membrane direct ethanol fuel cells. *Energy Environ. Sci.* **2011**, *4*, 1428–1433.

[26] Dutta, A.; Datta, J. Outstanding catalyst performance of PdAuNi nanoparticles for the anodic reaction in an alkaline direct ethanol (with anion-exchange membrane) fuel cell. *J. Phys. Chem. C* **2012**, *116*, 25677–25688.

[27] Jiang, R. Z.; Tran, D. T.; McClure, J. P.; Chu, D. A class of (Pd–Ni–P) electrocatalysts for the ethanol oxidation reaction in alkaline media. *ACS Catal.* **2014**, *4*, 2577–2586.

[28] Yi, Q. F.; Chu, H.; Chen, Q. H.; Yang, Z.; Liu, X. P. High performance Pd, PdNi, PdSn and PdSnNi nanocatalysts supported on carbon nanotubes for electrooxidation of C2–C4 alcohols. *Electroanal* **2015**, *27*, 388–397.

[29] Jongsomjit, S.; Prapainainar, P.; Sombatmankhong, K. Synthesis and characterisation of Pd–Ni–Sn electrocatalyst for use in direct ethanol fuel cells. *Solid State Ion*cs **2016**, *288*, 147–153.

[30] Jana, R.; Dhiman, S.; Peter, S. C. Facile solvothermal synthesis of highly active and robust $Pd_{1.87}Cu_{0.11}Sn$ electrocatalyst towards direct ethanol fuel cell applications. *Mater. Res. Express* **2016**, *3*, 084001.

[31] Rostami, H.; Abdollahi, T.; Mehdipour, P.; Rostami, A. A.; Farmanzadeh, D. Effect of Ni addition on electrocatalytic activity of PdCu catalysts for ethanol electrooxidation: An experimental and theoretical study. *Int. J. Hydrogen Energy* **2017**, *42*, 24713–24725.

[32] Yang, H. L.; Yu, Z. N.; Li, S. W.; Zhang, Q. L.; Jin, J.; Ma, J. T. Ultrafine palladium-gold-phosphorus ternary alloyed nanoparticles anchored on ionic liquids-noncovalently functionalized carbon nanotubes with excellent electrocatalytic property for ethanol oxidation reaction in alkaline media. *J. Catal.* **2017**, *353*, 256–264.

[33] Zhang, Y. Y.; Yi, Q. F.; Deng, Z. L.; Zhou, X. L.; Nie, H. D. Excellent electroactivity of ternary Pd–Ag–Sn nanocatalysts for ethanol oxidation. *Catal. Lett.* **2018**, *148*, 1190–1201.

[34] Shu, Y. L.; Shi, X. Q.; Ji, Y. Y.; Wen, Y.; Guo, X. Y.; Ying, Y.; Wu, Y. P.; Yang, H. F. Hollow echinus-like PdCuCo alloy for superior efficient catalysis of ethanol. *ACS Appl. Mater. Interfaces* **2018**, *10*, 4743–4749.

[35] Huang, Y. Y.; Guo, Y. L.; Wang, Y. B.; Yao, J. N. Synthesis and performance of a novel PdCuPb/C nanocatalyst for ethanol electrooxidation in alkaline medium. *Int. J. Hydrogen Energy* **2014**, *39*, 4274–4281.

[36] Bambagioni, V.; Bianchini, C.; Filippi, J.; Oberhauser, W.; Marchionni, A.; Vizza, F.; Psaro, R.; Sordelli, L.; Foresti, M. L.; Innocenti, M. Ethanol oxidation on electrocatalysts obtained by spontaneous deposition of palladium onto nickel-zinc materials. *ChemSusChem* **2009**, *2*, 99–112.

[37] Grimmer, C.; Grandi, M.; Zacharias, R.; Cermenek, B.; Weber, H.; Morais, C.; Napporn, T. W.; Weinberger, S.; Schenk, A.; Hacker, V. The electrooxidation of borohydride: A mechanistic study on palladium (Pd/C) applying RRDE, ^{11}B-NMR and FTIR. *Appl*. *Catal*. *B Environ*. **2016**, *180*, 614–621.

[38] Reetz, M. T.; Lopez, M. Method for *in situ* immobilization of water-soluble nanodispersed metal oxide colloids. U.S. Patent 7,244,688, July 17, 2007.

[39] Piasentin, R. M.; Spinacé, E. V.; Tusi, M. M.; Oliveira Neto, A. Preparation of PdPtSn/C-Sb_2O_5. SnO_2 electrocatalysts by borohydride reduction for ethanol electro-oxidation in alkaline medium. *Int*. *J*. *Electrochem*. *Sci*. **2011**, *6*, 2255–2263.

[40] Grimmer, C.; Zacharias, R.; Grandi, M.; Cermenek, B.; Schenk, A.; Weinberger, S.; Mautner, F. A.; Bitschnau, B.; Hacker, V. Carbon supported ruthenium as anode catalyst for alkaline direct borohydride fuel cells. *J*. *Phys*. *Chem*. *C* **2015**, *119*, 23839–23844.

[41] Grimmer, C.; Zacharias, R.; Grandi, M.; Pichler, B.; Kaltenboeck, I.; Gebetsroither, F.; Wagner, J.; Cermenek, B.; Weinberger, S.; Schenk, A. et al. A membrane-free and practical mixed electrolyte direct borohydride fuel cell. *J*. *Electrochem*. *Soc*. **2016**, *163*, F278–F283.

[42] Grimmer, C.; Grandi, M.; Zacharias, R.; Weinberger, S.; Schenk, A.; Aksamija, E.; Mautner, F. A.; Bitschnau, B.; Hacker, V. Carbon supported nanocrystalline manganese oxide: Surpassing platinum as oxygen reduction catalyst in direct borohydride fuel cells. *J*. *Electrochem*. *Soc*. **2016**, *163*, F885–F890.

[43] Cerritos, R. C.; Guerra-Balcázar, M.; Ramírez, R. F.; Ledesma-García, J.; Arriaga, L. G. Morphological effect of Pd catalyst on ethanol electro-oxidation reaction. *Materials* **2012**, *5*, 1686–1697.

[44] Wang, L. Q.; Lavacchi, A.; Bevilacqua, M.; Bellini, M.; Fornasiero, P.; Filippi, J.; Innocenti, M.; Marchionni, A.; Miller, H. A.; Vizza, F. Energy efficiency of alkaline direct ethanol fuel cells employing nanostructured palladium electrocatalysts. *ChemCatChem* **2015**, *7*, 2214–2221.

[45] Amin, R. S.; Abdel Hameed, R. M.; El-Khatib, K. M.; Elsayed Youssef, M. Electrocatalytic activity of nanostructured Ni and Pd-Ni on Vulcan XC-72R carbon black for methanol oxidation in alkaline medium. *Int*. *J*. *Hydrogen Energy* **2014**, *39*, 2026–2041.

[46] Simões, M.; Baranton, S.; Coutanceau, C. Influence of bismuth on the structure and activity of Pt and Pd nanocatalysts for the direct electrooxidation of $NaBH_4$. *Electrochim*. *Acta* **2010**, *56*, 580–591.

[47] Obradović, M. D.; Stančić, Z. M.; Lačnjevac, U. Č; Radmilović, V. V.; Gavrilović-Wohlmuther, A.; Radmilović, V. R.; Gojković, S. L. Electrochemical oxidation of ethanol on palladium-nickel nanocatalyst in alkaline media. *Appl*. *Catal*. *B Environ*. **2016**, *189*, 110–118.

[48] Shinozaki, K.; Zack, J. W.; Richards, R. M.; Pivovar, B. S.; Kocha, S. S. Oxygen reduction reaction measurements on platinum electrocatalysts utilizing rotating disk electrode technique. *J*. *Electrochem*. *Soc*. **2015**, *162*, F1144–F1158.

[49] Pollet, B. G.; Goh, J. T. E. The importance of ultrasonic parameters in the preparation of fuel cell catalyst inks. *Electrochim*. *Acta* **2014**, *128*, 292–303.

[50] Casella, I. G.; Contursi, M. Characterization of bismuth adatom-modified palladium electrodes: The electrocatalytic oxidation of aliphatic aldehydes in alkaline solutions. *Electrochim*. *Acta* **2006**, *52*, 649–657.

[51] Sekol, R. C.; Carmo, M.; Kumar, G.; Gittleson, F.; Doubek, G.; Sun, K.; Schroers, J.; Taylor, A. D. Pd–Ni–Cu–P metallic glass nanowires for methanol and ethanol oxidation in alkaline media. *Int*. *J*. *Hydrogen Energy* **2013**, *38*, 11248–11255.

[52] Paschos, O.; Simonov, A. N.; Bobrovskaya, A. N.; Hantel, M.; Rzepka, M.; Dotzauer, P.; Popov, A. N.; Simonov, P. A.; Parmon, V. N.; Stimming, U. Bismuth modified Pd/C as catalysts for hydrogen related reactions. *Electrochem*. *Commun*. **2010**, *12*, 1490–1492.

[53] Hofstead-Duffy, A. M.; Chen, D. J.; Sun, S. G.; Tong, Y. J. Origin of the current peak of negative scan in the cyclic voltammetry of methanol electro-oxidation on Pt-based electrocatalysts: A revisit to the current ratio criterion. *J*. *Mater*. *Chem*. **2012**, *22*, 5205–5208.

[54] Zhao, Y. Z.; Li, X. M.; Schechter, J. M.; Yang, Y. A. Revisiting the oxidation peak in the cathodic scan of the cyclic voltammogram of alcohol oxidation on noble metal electrodes. *RSC Adv*. **2016**, *6*, 5384–5390.

[55] Brouzgou, A.; Podias, A.; Tsiakaras, P. PEMFCs and AEMFCs directly fed with ethanol: A current status comparative review. *J*. *Appl*. *Electrochem*. **2013**, *43*, 119–136.

[56] Mondal, A.; De, A.; Datta, J. Cost effective and energy efficient catalytic support of Co and Ni in Pd matrix toward ethanol oxidation reaction: Product analysis and mechanistic interpretation. *Appl*. *Catal*. *A: Gen*. **2018**, *561*, 87–95.